Accepted Manuscript

Title: Carbon nanofiber-supported PdNi alloy nanoparticles as highly efficient bifunctional catalysts for hydrogen and oxygen evolution reactions

Authors: Jiawei Chen, Jiadong Chen, Danni Yu, Ming Zhang, Han Zhu, Mingliang Du

Please cite this article as: Jiawei Chen, Jiadong Chen, Danni Yu, Ming Zhang, Han Zhu, Mingliang Du, Carbon nanofiber-supported PdNi alloy nanoparticles as highly efficient bifunctional catalysts for hydrogen and oxygen evolution reactions, Electrochimica Actahttp://dx.doi.org/10.1016/j.electacta.2017.06.047

This is a PDF file of an unedited manuscript that has been accepted for publication. As a service to our customers we are providing this early version of the manuscript. The manuscript will undergo copyediting, typesetting, and review of the resulting proof before it is published in its final form. Please note that during the production process errors may be discovered which could affect the content, and all legal disclaimers that apply to the journal pertain.

Carbon nanofiber-supported PdNi alloy nanoparticles as highly efficient bifunctional catalysts for hydrogen and oxygen evolution reactions

Jiawei Chen, Jiadong Chen, Danni Yu, Ming Zhang*, Han Zhu, Mingliang Du

College of Materials and Textiles, Zhejiang Sci-Tech University, Hangzhou 310018, PR China;

Tel: 86-571-86843255; Fax: 86-571-86843255; E-mail: zhangming@zstu.edu.cn

Highlights

- The PdNi/CNF catalyst was synthesized by facile electrospinning and carbonization processes.

- The PdNi/CNF mats were directly employed as highly efficient bifunctional catalysts for the HER and OER.

- The hybrid materials exhibited high catalytic activity and long-term stability during the HER and OER.

- We offer an effective and feasible method for generating hydrogen by water electrolysis.

Abstract

Efficient bifunctional electrocatalysts for the hydrogen evolution reaction (HER) and oxygen evolution reaction (OER) must be developed to realize an inexpensive water-splitting system for large-scale applications. Herein, a novel PdNi carbon nanofiber (PdNi/CNF) catalyst was

synthesized by facile electrospinning and carbonization processes. The size and homogeneity of

the Pd−Ni alloy nanoparticles (NPs) could be effectively tuned by controlling the molar feed ratio

of metal precursors .The morphology and structure of the PdNi/CNFs were characterized, and the

working electrodes fabricated from the prepared catalyst mats were directly employed in the HER

and OER. The PdNi/CNFs-1:2 catalyst exhibits high catalytic activity in the HER with a low

overpotential of 55 mV at a current density of 10 mA cm^{-2} in an acidic solution. Moreover, under

1 M KOH electrolyte, an overpotential of 187 mV is required in the HER over the catalyst to

arrive 10 mA cm^{-2} and an overpotential of 289 mV is achieved in the OER at the same current

density. The superior HER and OER activities of the PdNi/CNFs are attributed to the synergistic

effects of the PdNi alloy nanoparticles (NPs) assembled on the CNFs. This work provides a simple

route for synthesizing highly efficient bifunctional electrocatalysts from 3d transition metals and a

small amount of noble metals for hydrogen and oxygen evolution reactions.

1. Introduction

Currently, much attention is focused on developing highly efficient and clean renewable

energy technologies to satisfy increasing energy demands and mitigate environmental

problems [1-3]. It is well known that generating hydrogen by water electrolysis is a key

strategy for overcoming these energy challenges [4-6]. However, the water-splitting

half-reactions, namely the hydrogen evolution reaction (HER) and oxygen evolution

reaction (OER), have high overpotentials and are energy intensive [7, 8]. Effective

electrocatalysts are essential to enhance the performance of electrochemical water splitting.

In particular, noble metal catalysts, such as Pt and RuO_2, have been employed as

state-of-the-art electrocatalysts for HER and OER, respectively [9, 10]. However, the high

cost and low global reserves of these metals prohibit their wide practical application.

Additionally, a catalyst that can simultaneously drive HER and OER is well desirable,

which is a fundamental demand as a highly efficient energy conversion device in water

splitting. Unfortunately, it is relatively difficult to develop the efficient, durable and

cost-effective bifunctional catalysts for the HER and OER. Therefore, the highly efficient

bifunctional catalysts with both high HER and OER activities are still high desired.

 To meet this objective while still exploiting the remarkable catalytic properties of noble

metals, they can be combined with 3d transition metals in small amounts. Some studies

indicate that 3d transition metals (e.g., nickel [11], cobalt [12] and tungsten [13]) have

relatively high electrocatalytic activities. However, most transition metals readily

precipitate after intermetallic aggregation and are corroded by electrolyte solutions over a

broad pH range, leading to a decrease in their catalytic performance. Of the different

transition metal materials, nickel (Ni) and its alloys or core-shell nanostructures have

received much attention due to their excellent corrosion resistance [11, 14]. Furthermore,

other studies showed that alloying Ni with other metals or forming the core-shell

nanoparticles, such as noble metals [14]; immobilizing Ni on a carbon surface; or using a

Ni material with a large active surface area significantly increased its activity in water

3

electrolysis. For instance, Hong Nhan Nong et al. synthesized IrNiOx core-shell nanoparticles for efficient electrochemical water splitting and exhibited the excellent OER activity [11].

Of the noble metals, palladium (Pd) is a promising catalyst for replacing platinum (Pt) because of its favorable catalytic properties, high electrochemical stability and relatively adequate reserves [15]. Therefore, due to its higher chemical resistance and high electrochemical activity [16], it is expected that modifying Ni with Pd might result in a highly stable HER and OER bifunctional catalyst. Additionally, the strong synergistic electronic effects of stable PdNi alloys are expected to prevent hydrogen adsorption on the bimetallic catalyst and reduce the HER overpotential. As an example, Ramazan Solmaz et al. successfully prepared Pt-modified electrocatalysts with the combination of the Ni-deposited carbon felt and thus optimize the electrochemical performance for the HER [17]. Therefore, PdNi alloys are promising bifunctional electrocatalysts for water electrolysis.

Carbonaceous materials such as graphene [18] and carbon nanotubes [19] have been widely used as conductive electrocatalyst supports. The size, shape and other properties of metal nanoparticles (NPs) can be efficiently tailored by fabricating them on carbon-based materials, which enables their uniform dispersion on the surface and prevents their aggregation during catalytic reactions [20]. Recently, carbon nanofibers (CNFs) have attracted much attention due to their desirable mechanical properties, remarkable physical and chemical resistances, and superior electrical and thermal conductivities [20]. K. Saranya et al. embedded the Fe-Ni nanoparticles into CNFs and demonstrated desirable

4

power conversion efficiency [21]. And Zhu *et al*. reported the preparation of $Co_9S_8@MoS_2$

core-shell particles on CNFs and used them as a highly efficient bifunctional catalyst for

H_2 and O_2 evolution [22]. It should be noted that 3D cross-linked CNF architectures are

conductive substrates on which the size, shape and distribution of NPs can be tailored.

They also have more effective reactive active sites for the supported NPs, providing higher

electrode surface areas as well as possess high electrical conductivity for charge transfer

[23, 24]. To our knowledge, the preparation of novel alloy NPs derived from Pd and the

transition metal on CNF supports for use as bifunctional electrocatalysts has rarely been

reported. Electrocatalysts fabricated on CNFs do not need to be coated on a glassy carbon

electrode; they can be directly utilized as electrodes, making them suitable for large-scale

applications.

In this work, PdNi alloy NPs were prepared on carbon nanofibers (PdNi/CNFs) by facile

electrospinning and thermal carbonization processes. Specifically, these materials were

fabricated by the stepwise heating of the non-toxic polyvinyl alcohol (PVA) nanofibrous

mat with the additions of Pd and Ni. The resulting three-dimensional (3D) PdNi/CNF

architectures provide the bifunctional electrocatalyst with good activity and stability in

both the HER and OER. The PdNi/CNF catalyst, which has a small Pd content, exhibits

excellent HER activity with a low overpotential of 55 mV (at j = 10 mA cm^{-2}), small Tafel

slope of 57 mV dec^{-1} and can be used continuously over 36 h in an acidic medium. And the

PdNi/CNF catalyst possesses good HER performance in a base electrolyte. Furthermore,

the PdNi/CNF catalyst has an onset potential of 1.560 V, overpotential of 289 mV and

long-term stability of up to 36 h in a 1.0 M KOH electrolyte solution during the OER.

Thus, the prepared bifunctional electrocatalysts provide a new route for achieving highly efficient electrochemical hydrogen production via water splitting.

2. Experiments

2.1. Materials

All the reagents were employed as received without further purification. Polyvinyl alcohol (PVA) and nickel nitrate hexahydrate ($NiN_2O_6 \cdot 6H_2O$, 98%) were obtained from Shanghai Aladdin Industrial Co., Ltd. Palladium chloride ($PdCl_2$, 59.8%) was purchased from Beijing HWRK Chemical Technology Co., Ltd. Deionized water (Milli-Q) was used in all the experiments.

2.2. PVA nanofibrous mat preparation

In a typical synthesis procedure, PVA nanofibers with Pd and Ni nanoparticles immobilized on the surface were prepared by electrospinning. First, 1.2 g PVA powder were dissolved in 10 mL deionized water in an Erlenmeyer flask under vigorous magnetic stirring until a uniform solution was obtained. The PVA mass fraction in the deionized water was 10%. Then, 50 mg $PdCl_2$ were added to the PVA aqueous solution. After stirring for 30 mins, 100 mg $NiN_2O_6 \cdot 6H_2O$ was immediately added dropwise to the resulting mixture, which was then stirred for 10 hours to give the PdNi nanoparticles (PdNi NPs)-PVA precursor solution. Various precursor solutions were prepared by adding different amounts of $PdCl_2$ and $NiN_2O_6 \cdot 6H_2O$ to the PVA aqueous solution according to the same method. Six precursor solutions with different Pd/Ni ratios were prepared.

PVA nanofiber mats containing PdNi NPs were obtained by electrospinning onto a piece of aluminum foil with a metallic roller. Specifically, the precursor solution was transferred

6

to an injection syringe with a stainless copper needle tip. The needle was linked to a

high-voltage DC power supply. The voltage, solution flow rate and needle-to-collector

distance were 12 kV, 0.5 mL h^{-1} and 12 cm, respectively. All the procedures were

performed at room temperature.

2.3. PdNi/CNF, Pd/CNF and Ni/CNF mat synthesis

The as-spun PVA nanofiber mats were carbonized in a chemical vapor deposition (CVD)

tube furnace using the following heating program. The nanofiber mats were first heated to

230 °C in air at a rate of 5 °C min^{-1} and then kept at that temperature for 60 min for

pre-oxidation and stabilization. One hour after the heating process started, Ar gas (150

sccm) was flowed into the system. Then, the samples were heated to 900 °C (5 °C min^{-1})

under Ar and maintained at that temperature for 180 min to obtain a stacked polyaromatic

carbon (graphitic) structure. The samples were subsequently cooled to room temperature.

The resulting PdNi/CNF samples contained 100 mg PdCl$_2$ and 50 mg NiN$_2$O$_6$·6H$_2$O, 75

mg PdCl$_2$ and 75 mg NiN$_2$O$_6$·6H$_2$O, 50 mg PdCl$_2$ and 100 mg NiN$_2$O$_6$·6H$_2$O, and 30 mg

PdCl$_2$ and 120 mg NiN$_2$O$_6$·6H$_2$O and were denoted by PdNi/CNFs-1:0.5, PdNi/CNFs-1:1,

PdNi/CNFs-1:2, and PdNi/CNFs-1:4, respectively. Pd/CNFs and Ni/CNFs were also

prepared and carbonized under the same conditions as controls.

2.4. Material characterization

The sample morphologies were observed using a JSM-6700F field-emission scanning

electron microscope (FE-SEM; JEOL, Japan) operated at an accelerating voltage of 3 kV.

TEM images and selected-area electron diffraction (SAED) patterns of the samples were

obtained on a JSM-2100 transmission electron microscope (TEM; JEOL, Japan) at an

7

accelerating voltage of 200 kV. High-angle annular dark field scanning transmission electron microscopy (HAADF-STEM), STEM, and energy-dispersive X-ray (EDX) line scans were obtained using an STEM instrument (Tecnai G2 F30 S-Twin, Philips-FEI) at an accelerating voltage of 300 kV. The X-ray diffraction (XRD) patterns of the samples were recorded by a Bruker AXS D8 X-ray diffractometer over the 2θ range of 10° to 80° using a step size of 0.02° and Cu Kα radiation (λ = 0.15406 nm). X-ray photoelectron spectra of all the samples were obtained using an X-ray photoelectron spectrometer (Kratos Axis Ultra DLD) operated at 15 kV with aluminum Kα radiation (1486.6 eV).

2.5. Electrochemical measurements

The electrochemical measurements for the HER and OER were performed at room temperature using a typical three-electrode cell controlled by a CHI 660E electrochemical workstation. Saturated calomel electrodes (E(RHE) = E(SCE) + 0.244 V + 0.059×pH after calibration) was used as the reference electrodes. To avoid influencing the HER catalytic property of tested samples, graphitic electrode was used as the counter electrode during HER activity tests. Pt mesh electrode was used as the counter electrode in OER tests. The working electrode was fabricated by cutting a sample into squares with proper size and then fixing them in a Teflon electrode clamp. The electrolyte solution was 0.5 M H_2SO_4 for HER or 1 M KOH for HER and OER, respectively. Before each test, nitrogen was bubbled through the electrolyte solution to eliminate the dissolved oxygen. The working electrodes were used as negative and positive electrodes for the HER and OER, respectively. Furthermore, the electrochemical performance of a commercial Pt/C (20 wt%) catalyst in the HER and a commercial RuO_2 catalyst during the OER were measured as comparison,

8

respectively. Cyclic voltammetry (CV) was performed to activate and stabilize the

catalysts, and linear sweep voltammetry (LSV) was performed at a scan rate of 5 mV s^{-1} to

measure the HER and OER catalytic activities. In addition, the polarization curves were

measured after IR compensation. Electrochemical impedance spectroscopy (EIS) was

conducted over the frequency range of 10^{-1}-10^5 Hz at constant voltages of -0.1 V vs RHE

for the HER and 1.6 V vs RHE for the OER. The catalytic stability in the HER and OER

was determined by measuring the chronoamperometric response curves at a constant

voltage.

3. Results and discussion

The FE-SEM and TEM results show that large, non-uniformly distributed Pd (Fig. 1a-b)

and Ni NPs (Fig. 1c-d) form on the Pd/CNFs and Ni/CNFs, respectively. However, PdNi

alloy NPs with an average diameter of only ca. 8 nm are evenly distributed on the CNFs in

PdNi/CNFs-1:2, as shown by the FE-SEM and TEM images in Fig. 1e and 1f, respectively.

Furthermore, no aggregation is observed, indicating that the NP size and dispersion can be

effectively tailored by the formation of the PdNi alloy structure. A comparison of the

morphologies of these samples of different Pd/Ni molar feed rations (Fig. S1) reveals that

PdNi/CNFs-1:2 has the optimal nanoparticle size distribution. Furthermore, as shown in

Fig. 1e, the thermal carbonization process results in the formation of 3D conductive CNF

networks, which are essential for effectively supporting and immobilizing the PdNi alloy

NPs.

The high-resolution TEM (HRTEM) image in Fig. 1f clearly shows the PdNi alloy

crystalline structure, which indicates that PdNi alloy NPs have a high crystallinity, chiseled

9

lattice fringes and mightily immobilized in the CNFs. The NP d-spacing of PdNi/CNFs

indicated by the yellow arrows in the figure was determined to be 0.216 nm between the

values of Pd/CNFs (0.224 nm) and Ni/CNFs (0.204 nm), which corresponds to the (111)

plane of face-centered cubic (fcc) crystals.

The morphology of PdNi/CNFs-1:2 can be determined from the HAADF-STEM image

in Fig. 2a. Most of the PdNi alloy nanocrystals are uniformly distributed and supported on

the CNF surface. As shown in Fig. 2b, the STEM-EDS mapping analysis reveals the

presence of the C, O, Pd and Ni, and the C and the slight O elements are derived from the

CNF substrate. The distributions of Pd and Ni match well, verifying the successful

preparation of an alloy and the absence of separate Pd and Ni phases. Carbon is distributed

over the entire CNF substrate, and relatively small amounts of oxygen are detected. The

SAED pattern of PdNi/CNFs-1:2 shown in Fig. 2c further reveals the PdNi alloy NP has an

order crystal structure, which enables strong electronic coupling due to synergistic effects

and thus results in a highly efficient bifunctional catalyst. The NPs are polycrystalline

nanocrystals, as shown by the circular patterns that correspond to the (111), (220) and

(200) planes of fcc crystals. The lattice distances were determined from the SAED pattern

and are in agreement with the HRTEM results. Additionally, the EDX line-scan analysis of

the NPs shows that Pd and Ni are distributed over the entire surface, and their signal

intensities in the line scans vary correspondingly, strongly indicating that a crystalline alloy

structure is obtained (Fig. 2d).

To determine the crystal structures of the bifunctional catalysts, XRD measurements

were performed. As shown in Fig. 3a and Fig. S2, all the sample with varying Pd/Ni ratios

exhibit a broad peak at approximately 24.1°, which is attributed to the (002) planes of

graphitic carbon. The diffraction patterns of the Pd/CNFs and Ni/CNFs are consistent with

those of fcc Pd (JCPDS No. 65-6174) and fcc Ni (JCPDS No. 65-2865), respectively. The

(111) d-spacings obtained from the XRD patterns using Bragg's law are in good agreement

with those obtained from the previous HRTEM results. The three peaks in the

PdNi/CNFs-1:2 XRD pattern (Fig. 3a) at 42.4°, 49.5° and 74.1° correspond to the (111),

(200) and (220) planes, respectively. The PdNi/CNFs-1:2 diffraction peaks appear at

slightly lower 2θ values than the Ni/CNF peaks because the Ni cell parameters increase

upon alloy formation. In contrast, the PdNi/CNFs-1:2 diffraction peaks appear at higher

angles than the Pd/CNF peaks, indicating that the lattice parameter decreases when the

larger Pd atoms are partially replaced by the smaller Ni atoms, which strongly confirms the

formation of a PdNi alloy with isomorphous structure [25, 26]. The XRD results of

Pd-Ni/CNFs with different Pd/Ni molar ratios (i.e., 1:0.5 to 1:4) show that there are only

three diffraction peaks located at diffraction angles between these of Pd/CNFs (the 2θ

values: 40.4°, 46.9° and 68.3°, respectively) and Ni/CNFs (the 2θ values: 44.7°, 52.2° and

76.3°, respectively), indicating that no phase separation appeared and all the samples are

PdNi alloy.

To determine the chemical structures and compositions of the samples, the XPS survey

spectra of the Pd/CNFs, Ni/CNFs and PdNi/CNFs-1:2 were obtained. All the spectra were

calibrated to the C 1s peak at 284.2 eV. As shown in Fig. 3b, the PdNi/CNFs-1:2 XPS

spectrum exhibits peaks corresponding to the Pd, Ni, C and O, and the response present of

the C and O is attributed to the CNF substrate. In the Pd 3d spectrum of PdNi/CNFs-1:2

11

(Fig. 3c), two pronounced peaks are observed at approximately 341.9 eV (Pd $3d_{5/2}$) and

335.8 eV (Pd $3d_{7/2}$, relatively weaker). The Pd 3d peaks of the PdNi/CNFs are shifted to

higher binding energies (BEs) relative to those of the Pd/CNFs, due to electron transfer

from Pd to Ni during the alloying process [27]. Meanwhile, the Ni 2p spectrum of

PdNi/CNFs-1:2 exhibits two obvious peaks at approximately 872.3 eV and 854.5 eV (Fig.

3d) and the BEs of Ni 2p shift to higher values, which is ascribed to the transform of the

electron and crystal structure by the Pd incorporation [27]. Thus, these results further

demonstrate the successful synthesis of PdNi alloy NPs on CNFs.

    Water splitting comprises the half-reactions HER and OER, which generate hydrogen by

water electrolysis [2, 7, 28]. To measure the HER performance of PdNi/CNFs-1:2, the

electrocatalytic activity was measured in an Ar-saturated 0.5 M H_2SO_4 electrolyte using a

standard three-electrode electrochemical cell. For comparison, the electrocatalytic

performances of a commercial Pt/C catalyst, the Pd/CNFs and the Ni/CNFs were also

measured. As expected, the Pt/C catalyst exhibits excellent HER activity with an onset

potential of nearly zero (Fig. 4a) and a very small Tafel slope of 36 mV dec^{-1} (Fig. 4b),

which is consistent with previous results [29]. As shown in Fig. 4a, the PdNi/CNFs-1:2

catalyst has a very low onset potential of 26 mV, which is even closer to that of the Pt/C

catalyst. Moreover, PdNi/CNFs-1:2 has a relatively low overpotential of 55 mV at a

current density of 10 mA cm^{-2} (Table 1). In comparison, the Pd/CNFs and Ni/CNFs have

higher overpotentials of 101 and 167 mV, respectively, at the same current density. To

further assess the HER performance of PdNi/CNFs-1:2, the Tafel equation was fitted to

data obtained from the polarization curves to determine the Tafel slopes (Fig. 4b) and the

open circuit potential (OCP) values of the electrocatalysts were listed in the Table 1. It

should be noted that the Tafel slope of PdNi/CNFs-1:2 (57 mV dec^{-1}, Table 1) is much

smaller than those of both the Pd/CNFs (140 mV dec^{-1}) and Ni/CNFs (164 mV dec^{-1}) and

is similar to that of the Pt/C catalyst (36 mV dec^{-1}). This small Tafel slope indicates that

the electrocatalytic process follows the Volmer-Heyrovsky mechanism in which the

electrochemical desorption step (Heyrovsky reaction) is the rate-limiting step [30]. The

small Tafel slope of Pd/Ni-CNFs-1:2 is favorable for large-scale practical applications

because small increases in the overpotential lead to significant increases in the current

density [31]. To visually observe the needed overpotential to arrive a current density of 10

mA cm^{-2}, Fig. 4c is plotted and it can be seen that PdNi/CNFs-1:2 catalyst needs lower

overpotential than Pd/CNFs and Ni/CNFs. To analyze the effect of the alloy composition

on the HER performance, the catalytic performances of PdNi/CNFs-1:0.5, PdNi/CNFs-1:1

and PdNi/CNFs-1:4 in 0.5 M H_2SO_4 were also measured as described previously. As

shown in Fig. S3a-b, PdNi/CNFs-1:2 exhibits the optimal HER activity with lower

overpotential and smaller Tafel slope. The HER activity for the PdNi/CNFs-1:2 is

favorably compared with recently reported electrocatalysts with similar composition or

structure (Table S1).

As for the HER activity, exchange current density (j_0) is an essential metrics by

indicating the inherent performance of the catalyst and reflecting the surface active area.

The j_0 values were calculated from the extrapolation of Tafel plot for all the samples with

different Pd/Ni molar ratios. The j_0 for the PdNi/CNFs-1:2 comes to 1.536 mA cm^{-2}, which

is higher than that for the other products. The obvious increase of the j_0 value for the

13

bifunctional electrocatalysts demonstrates outstanding catalytic properties in the HER

process owing to a large number of active sites exposed to the surface of electrode

materials.

The double-layer capacitances (C_{dl}) were measured to determine the intrinsic catalytic

activity and electrocatalytically active catalyst surface areas [32]. The inset in Fig. 4d show

the CV plots of PdNi/CNFs-1:2 measured in the potential range of 0.26-0.38 V vs RHE at

scan rates of 20-200 mV s^{-1} in the absence of a faradic current. CV plots of Pd/CNFs and

Ni/CNFs are shown in Fig. S3c and Fig. S3d, respectively. And the related fitting linear

curves of these three catalysts are displayed in Fig. 4d. The C_{dl} values of the Pd/CNFs,

Ni/CNFs and PdNi/CNFs-1:2 calculated from the different current density plots are listed

in Table 1 and the computing method of C_{dl} is explained in the supplementary information.

The PdNi/CNFs-1:2-based electrode has a higher C_{dl} (55.5 mF cm^{-2}) than the other tested

electrodes, showing that PdNi/CNFs-1:2 has the largest catalytically active surface area

due to the bimetallic alloy structure and the presence of more active sites. Thus, these

results further demonstrate that the prepared PdNi/CNFs-1:2 catalyst exhibits excellent

electrocatalytic activity and chemical stability in the HER.

It is well known that the Rct is strongly related to the HER kinetics [14, 33]. EIS

measurements were performed at η= -0.10 V vs RHE to study the HER kinetics and the

specific electrochemical impedance spectra fitting parameters are listed in Table 2. The

Nyquist plots without Warburg impedance for the Pd/CNFs, Ni/CNFs and PdNi/CNFs-1:2

are shown in Fig. 4e. According to the results of calculation, the charge transfer resistance

(Rct) of PdNi/CNFs-1:2 (23 Ω) is considerably lower than those of the Pd/CNFs (47 Ω)

14

and Ni/CNFs (321 Ω) as indicated in Table 2, indicating the available HER kinetics, which

is consistent with the higher catalytic activity observed for the corresponding electrode [30,

34]. In addition to having high catalytic activity, the catalyst must also exhibit long-term

stability during the HER process. As shown in Fig. 4f, the current density of

PdNi/CNFs-1:2 varies negligibly over 36 h of water electrolysis, demonstrating the good

stability of the catalyst.

In addition, the PdNi/CNFs-1:2 polarization curve obtained after an accelerated

degradation test of 1000 potential cycles is similar to the original curve (Fig. S4a), and

only a small loss in the catalytic activity is observed. Furthermore, the PdNi/CNFs-1:2 CV

curve decreases only slightly relative to the initial curve (inset in Fig. S4a). The

microstructure of the PdNi/CNFs electrode was examined by TEM after the stability

measurement. The TEM image in Fig. S4b shows that the PdNi alloy NPs do not aggregate

or detach from the support during the long-term test, clearly showing their chemical

stability during the HER.

It is well known that the OER overpotential is higher than the HER overpotential during

water splitting [22], because it involves four electron-transfer steps with undesirable

kinetics [35, 36]. In this work, the potential of our unique electrochemical system in the

OER was explored by measuring the OER activities of the samples in a 1 M KOH

electrolyte solution. The results reveal the exceptional OER performance of

PdNi/CNFs-1:2. The PdNi/CNFs exhibits outstanding OER performance with relatively

low overpotential among that of recently reported OER electrocatalysts (Table S2). As

shown in Fig. 5a, the onset potential of PdNi/CNFs-1:2 (approximately 1.56 V vs RHE) is

much smaller than those of the Pd/CNFs and Ni/CNFs. The overpotential at a current

density of 10 mA cm^{-2} is a significant performance metric for OER catalysts, correlating

closely to the current density of a solar-to-fuel conversion device with an efficiency of 10%

[22, 37]. The PdNi/CNFs-1:2 can induce a current density of 10 mA cm^{-2} at a low

overpotential of 289 mV. In comparison, the corresponding Pd/CNF and Ni/CNF

overpotentials are 348 and 380 mV, respectively. The Tafel plots of the overpotential vs

the current density were constructed to further examine the OER kinetics (Fig. 5b). The

Tafel slopes of the PdNi/CNFs-1:2, the Pd/CNFs, the Ni/CNFs and the commercial RuO$_2$

catalyst are 117, 171, 184 and 115 mV dec^{-1}, respectively. The relatively small value for

the PdNi/CNFs even close to that of the state-of-the-art RuO$_2$ catalyst is strongly indicative

of their remarkable OER kinetics. The Ni substrate modifies the Pd electronic structure,

which might accelerate O−O bond formation and decrease the energy barrier of the

proton-coupled electron transfer in the OER [38]. And as a bifunctional catalyst, it is

necessary to evaluate their catalytic performance both to OER and HER in the same

electrolyte. Therefore, HER activities of catalysts are also measured in 1 M KOH and

corresponding results are shown in Fig. 5c-d. In 1 M KOH electrolyte, PdNi/CNFs still

have better HER performance than Pd/CNFs and Ni/CNFs. To arrive a current density of

10 mA cm^{-2}, PdNi/CNFs-1:2 only need an overpotential of 187 mV, much lower than

Pd/CNFs of 265 mV and Ni/CNFs of 345 mV. And the Tafel slope of PdNi/CNFs is 93

mV dec^{-1}, only bigger than Pt/C catalysts of 42 mV dec^{-1}. The above results indicate that

PdNi/CNFs show the best HER performance among Pd/CNFs, Ni/CNFs and

PdNi/CNFs-1:2. **T**he good HER and OER performance under alkaline condition show that

PdNi/CNFs-1:2 has a bright prospect in practical water splitting.

EIS measurements in OER were performed at 1.60 V vs RHE to calculate the Rct values

(Table 2), and the results are shown in Fig. 5e. PdNi/CNFs-1:2 clearly has a lower Rct (19

Ω) than the other prepared catalysts, and therefore, the OER kinetics of this catalyst are

more favorable. The results of this work indicate that PdNi/CNFs-1:2 exhibits excellent

catalytic activity with a low onset potential, overpotential and Tafel slope and can thus be

used for efficient electrochemical water splitting. In addition, the stability of the

PdNi/CNFs-1:2 catalyst was evaluated by measuring the time-dependent current density in

a 1 M KOH solution, and the results are shown in Fig. 5f. The PdNi/CNF current density

initially decreases during the OER, reaching a minimum of 40 mA cm^{-2} after

approximately 1 h. The current density changes negligibly over the following 35 h,

showing the excellent stability of the catalyst.

After a long-term water electrolysis test, the current density and CV curve of the

PdNi/CNFs decrease slightly, as shown in Fig. S4c, again indicating that the PdNi/CNFs

catalyst is stable during O_2 evolution. As the electrolysis time in an alkaline solution

increases, the PdNi alloy NPs might aggregate slightly, as indicated by TEM observations

of PdNi/CNFs-1:2 after the stability test (Fig. S4d).

In addition, the EDS and XRD patterns of the PdNi/CNFs-1:2 before and after 1000

potential cycles for HER and OER were obtained to better analyze and contrast the changes

of the composition and structure of the PdNi alloy NPs (Fig. S5). The EDS spectra for the

element content altering of Pd and Ni presented as a histogram form (Fig. S5a).The results

demonstrate that there is a drop of approximately 30% for the mass ratio of Pd and Ni after

1000 potential cycles for the HER and OER. It can be accounted for the slight dissolution

and corrosion during the HER and OER process. The decline content of Pd in the HER is

lower than the drop values in the OER, but the situation of Ni is opposite, indicating that

Pd element is more stable in acid condition than alkaline condition and Ni element is

opposite. Moreover, the diffraction characteristic peaks show almost no position shift

during the electrocatalytic process, leading to the remarkable stability and durability of the

PdNi/CNFs-1:2 as bifunctional electrocatalysts.

To explore the effect of the alloy composition on both HER and OER performance under

alkaline condition, both HER and OER catalytic performances of PdNi/CNFs-1:0.5,

PdNi/CNFs-1:1, PdNi/CNFs-1:2 and PdNi/CNFs-1:4 in 1 M KOH were also measured as

described previously (Fig. S6). As shown in Fig. S6a-b, PdNi/CNFs-1:2 exhibits the

optimal OER activity with lower overpotential and smaller Tafel slope. The OER activity

for the PdNi/CNFs-1:2 is favorably compared with recently reported electrocatalysts with

similar composition or structure (Table S2). Similarly, as shown in Fig. S6c-d,

PdNi/CNFs-1:2 still shows the best HER performance among all PdNi/CNFs with different

feed molar ratios of metal precursor in 1 M KOH electrolyte. The Tafel slope of

PdNi/CNFs-1:2 is only 93 mV dec^{-1} which is much lower than other PdNi/CNFs with

different molar ratios.

The good catalytic activity of the PdNi/CNFs in water splitting is attributed to the

following factors. (1) Alloying Ni and Pd alters their electronic structures and leads to the

formation of more accessible active sites. (2) The synergistic effects of the bimetallic PdNi

NPs result in high electrical conductivity and thus rapid charge transfer. (3) Ni is

embedded in the Pd crystalline phase, improving its corrosion resistance and

electrochemical stability. (4) The CNF substrate can facilitate gas diffusion during the

HER and OER and provide a large contact area between the electrolyte and active sites. In

this work, the PdNi/CNFs, which have a very low Pd content, act as remarkable

bifunctional electrocatalysts with high catalytic activities in the HER and OER. However,

this system must be further studied to determine the optimal alloy composition and identify

the specific HER and OER mechanisms. Future work will be focused on these problems.

4. Conclusions

In summary, a new class of the PdNi alloy structure was prepared on CNFs by

electrospinning and subsequent carbonization. The as-synthesized PdNi/CNFs, which have

a low Pd loading, exhibit superior catalytic activity and good stability in both the HER and

OER and are thus a promising alternative bifunctional electrocatalyst. The highly efficient

catalytic performance of the PdNi/CNFs is attributed to the synergistic effects of the PdNi

alloy and the properties of the CNF substrate. The combination of these factors enhances

the catalytic activity and is expected to enable the realization of cost-effective hydrogen

and oxygen generation. Therefore, the catalyst developed in this work could be suitable for

use in various water-splitting applications.

Acknowledgements

20

References:

[1] D. Strmcnik, P.P. Lopes, B. Genorio, V.R. Stamenkovic, N.M. Markovic, Design principles for hydrogen evolution reaction catalyst materials, Nano Energy, 29 (2016) 29-36.

[2] M. Tahir, N. Mahmood, X. Zhang, T. Mahmood, F.K. Butt, I. Aslam, M. Tanveer, F. Idrees, S. Khalid, I. Shakir, Y. Yan, J. Zou, C. Cao, Y. Hou, Bifunctional catalysts of Co_3O_4@GCN tubular nanostructured (TNS) hybrids for oxygen and hydrogen evolution reactions, Nano Res., 8 (2015) 3725-3736.

[3] F. Safizadeh, E. Ghali, G. Houlachi, Electrocatalysis developments for hydrogen evolution reaction in alkaline solutions, Int. J. Hydrogen Energy, 40 (2015) 256–274.

[4] E.J. Popczun, J.R. Mckone, C.G. Read, A.J. Biacchi, A.M. Wiltrout, N.S. Lewis, R.E. Schaak, nanostructured nickel phosphide as an electrocatalyst for the hydrogen evolution reaction, J. Am. Chem. Soc., 135 (2013) 9267.

[5] M.W. Kanan, D.G. Nocera, In situ formation of an oxygen-evolving catalyst in neutral water containing phosphate and Co^{2+}, Science, 321 (2008) 1072-1075.

[6] N.S. Mcintyre, M.G. Cook, X-ray photoelectron studies on some oxides and hydroxides of cobalt, nickel, and copper, Anal. Chem., 47 (1975) 2208-2213.

[7] A. Bergmann, I. Zaharieva, H. Dau, P. Strasser, Electrochemical water splitting by layered and 3D cross-linked manganese oxides: correlating structural motifs and catalytic activity, Energ. Environ. Sci., 6 (2013) 2745-2755.

[8] S.A. Khan, S.B. Khan, A.M. Asiri, Electro-catalyst based on cerium doped cobalt oxide for oxygen evolution reaction in electrochemical water splitting, J. Mater. Sci. Mater. El., 27 (2016) 1-9.

[9] Y. Lee, J. Suntivich, K.J. May, E.E. Perry, Y. Shao-Horn, Synthesis and activities of rutile IrO_2 and RuO_2 nanoparticles for oxygen evolution in acid and alkaline solutions, J. Phys. Chem. Lett., 3(2012) 399-404.

[10] J. Kibsgaard, T. F. Jaramillo, Molybdenum phosphosulfide: an active, acid-Stable, earth-abundant catalyst for the hydrogen evolution reaction, Angew. Chem., Int. Ed., 53 (2015) 14433-14437.

[11] H. N. Nong, H. S. Oh, T. Reier, E. Willinger, M. G. Willinger, V. Petkov, D. Teschner, P. Strasser, Oxide-supported IrNiO(x) core-shell particles as efficient, cost-effective, and stable catalysts for electrochemical water splitting, Angew. Chem. Int. Ed. Engl., 54 (2015) 2975-2981.

[12] M. Fayette, A. Nelson, R.D. Robinson, Electrophoretic deposition improves catalytic performance of Co_3O_4 nanoparticles for oxygen reduction/oxygen evolution reactions, J. Mater. Chem. A, 3 (2015) 4274-4283.

[13] K. Calfumán, M. García, Maria, X, J. Aguirre, B. Matsuhiro, L. Mendoza, M. Isaacs, Hydrothermal synthesis of monoclinic WO_3 nanoplates and nanorods used as an electrocatalyst for hydrogen evolution reactions from water, Chem. Eng. J., 165 (2010) 365-369.

[14] R. Solmaz, Electrochemical preparation and characterization of C/Ni–NiIr composite electrodes as novel cathode materials for alkaline water electrolysis, Int. J. Hydrogen Energy, 38 (2013) 2251-2256.

[15] B. Pierozynski, T. Mikolajczyk, M. Turemko, E. Czerwosz, M. Kozlowski, Hydrogen evolution reaction at Pd-modified carbon fibre in 0.1M NaOH, Int. J. Hydrogen Energy, 40

(2014) 1795–1799.

[16] J. Tang, Y. Zuo, Study on corrosion resistance of palladium films on 316L stainless steel by electroplating and electroless plating, Corros. Sci., 50 (2008) 2873-2878.

[17] R. Solmaz, A. Gündoğdu, A. Döner, G. Kardaş, The Ni-deposited carbon felt as substrate for preparation of Pt-modifiedelectrocatalysts: application for alkaline water electrolysis, Int. J. Hydrogen Energy, 37 (2012) 8917-8922.

[18] A.K. Geim, K.S. Novoselov, The rise of graphene, Nat. Mater., 6 (2007) 183-191.

[19] N.F. Khusnun, A.A. Jalil, S. Triwahyono, N.W. Jusoh, A. Johari, K. Kidam, Interaction between copper and carbon nanotubes triggers their mutual role in the enhanced photodegradation of p-chloroaniline, Phys. Chem. Chem. Phys., 18 (2016) 12323-12331.

[20] B. Pierozynski, T. Mikolajczyk, Hydrogen evolution reaction at Ru-modified carbon fibre in 0.5 M H_2SO_4, Int. J. Electrochem. Sci., 7 (2012) 9697-9706.

[21] K. Saranya, A. Subramania, N. Sivasankar, Influence of earth-abundant bimetallic (Fe–Ni) nanoparticle-embedded CNFs as a low-cost counter electrode material for dye-sensitized solar cells, RSC Adv., 5 (2015) 43611-43619.

[22] H. Zhu, J. Zhang, R. Yanzhang, M. Du, Q. Wang, G. Gao, J. Wu, G. Wu, M. Zhang, B. Liu, J. Yao, X. Zhang, When cubic cobalt sulfide meets layered molybdenum disulfide: a core-shell system toward synergetic electrocatalytic water splitting, Adv. Mater., 27 (2015) 4752-4759.

[23] Y. Su, Y. Zhu, H. Jiang, J. Shen, X. Yang, W. Zou, J. Chen, C. Li, Cobalt nanoparticles embedded in N-doped carbon as an efficient bifunctional electrocatalyst for oxygen reduction and evolution reactions, Nanoscale, 6 (2014) 15080-15089.

[24] F. Nitze, M. Mazurkiewicz, A. Malolepszy, A. Mikolajczuk, P. Kędzierzawski, C.W. Tai, G.

Hu, K.J. Kurzydłowski, L. Stobinski, A. Borodzinski, Synthesis of palladium nanoparticles decorated helical carbon nanofiber as highly active anodic catalyst for direct formic acid fuel cells, Electrochim. Acta, 63 (2012) 323-328.

[25] D. Wang, H.L. Xin, R. Hovden, H. Wang, Y. Yu, D.A. Muller, F.J. DiSalvo, H.D. Abruna, Structurally ordered intermetallic platinum-cobalt core-shell nanoparticles with enhanced activity and stability as oxygen reduction electrocatalysts, Nat. Mater., 12 (2013) 81-87.

[26] C. M. Chen, Q. Zhang, X. C. Zhao, B. Zhang, Q. Q. Kong, M. G. Yang, Q. H. Yang, M. Z. Wang, Y. G. Yang, R. Schlögl, D.S. Su, Hierarchically aminated graphene honeycombs for electrochemical capacitive energy storage, J. Mater. Chem., 22 (2012) 14076.

[27] H. Husin, W. N. Su, C. J. Pan, J. Y. Liu, J. Rick, S. C. Yang, W. T. Chuang, H. S. Sheu, B. J. Hwang, Pd/NiO core/shell nanoparticles on $La_{0.02}Na_{0.98}TaO_3$ catalyst for hydrogen evolution from water and aqueous methanol solution, Int. J. Hydrogen Energy, 38 (2013) 13529-13540.

[28] S. Cobo, J. Heidkamp, P.A. Jacques, J. Fize, V. Fourmond, L. Guetaz, B. Jousselme, V. Ivanova, H. Dau, S. Palacin, M. Fontecave, V. Artero, A janus cobalt-based catalytic material for electro-splitting of water, Nat. Mater., 11 (2012) 802-807.

[29] Y. Huang, Y.E. Miao, L. Zhang, W. W. Tjiu, J. Pan, T. Liu, Synthesis of few-layered MoS_2 nanosheet-coated electrospun SnO_2 nanotube heterostructures for enhanced hydrogen evolution reaction, Nanoscale, 6 (2014) 10673-10679.

[30] S. A. Vilekar, I. Fishtik, R. Datta, Kinetics of the hydrogen electrode reaction, J. Electrochem. Soc., 157 (2010) B1040.

[31] D. Merki, X. Hu, Recent developments of molybdenum and tungsten sulfides as hydrogen evolution catalysts, Energ. Environ.Sci., 4 (2011) 3878-3888.

[32] J. Chen, D. Yu, W. Liao, M. Zheng, L. Xiao, H. Zhu, M. Zhang, M. Du, J. Yao, WO_{3-x}

nanoplates grown on carbon nanofibers for an efficient electrocatalytic hydrogen evolution

reaction, ACS Appl. Mater. Interfaces, 8 (2016) 18132-18139.

[33] B. Pierozynski, Hydrogen evolution reaction at Pd-modified carbon fibre and nickel-coated

carbon fibre materials, Int. J. Hydrogen Energy, 38 (2013) 7733-7740.

[34] Y. Jin, P.K. Shen, Nanoflower-like metallic conductive MoO_2 as a high-performance

non-precious metal electrocatalyst for the hydrogen evolution reaction, J. Mater. Chem. A, 3

(2015) 20080-20085.

[35] M.S. Burke, M.G. Kast, L. Trotochaud, A.M. Smith, S.W. Boettcher, Cobalt–Iron (Oxy)

hydroxide oxygen evolution electrocatalysts: the role of structure and composition on activity,

stability, and mechanism, J. Am. Chem. Soc., 137 (2015) 3638.

[36] R.L. Doyle, I.J. Godwin, M.P. Brandon, M.E. Lyons, Redox and electrochemical water

splitting catalytic properties of hydrated metal oxide modified electrodes, Phys. Chem. Chem.

Phys., 15 (2013) 13737-13783.

[37] X. Long, J. Li, S. Xiao, K. Yan, Z. Wang, H. Chen, S. Yang, A strongly coupled graphene and

FeNi double hydroxide hybrid as an excellent electrocatalyst for the oxygen evolution

reaction, Angew. Chem., Int. Ed. Engl., 53 (2014) 7584–7588.

[38] Y. Surendranath, M.W. Kanan, D.G. Nocera, Mechanistic studies of the oxygen evolution

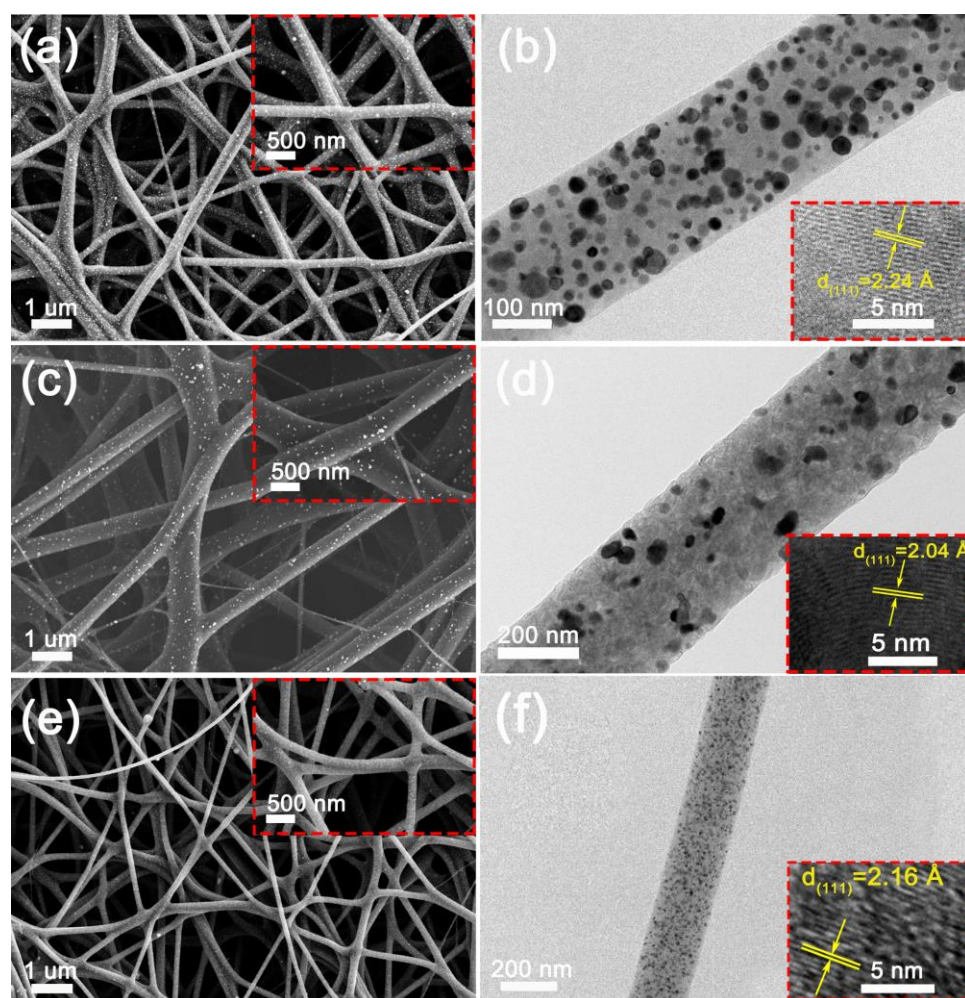reaction by a cobalt-phosphate catalyst at nseutral pH, J. Am. Chem. Soc., 132 (2010)

16501-16509.

Fig. 1 (a, c, e) FE-SEM and (b, d, f) TEM images of the Pd/CNFs (a, b), Ni/CNFs (c, d) and

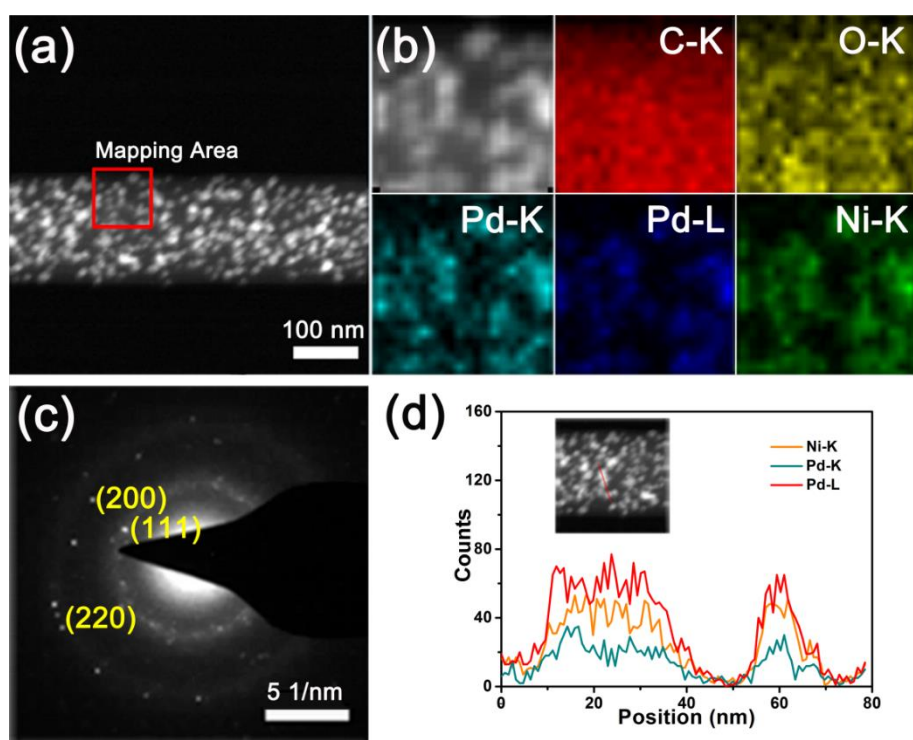PdNi/CNFs-1:2 (e, f). The insets are the corresponding HRTEM images.

Fig. 2 (a) HAADF-STEM and (b) STEM-EDS mapping images and (c) SAED pattern of

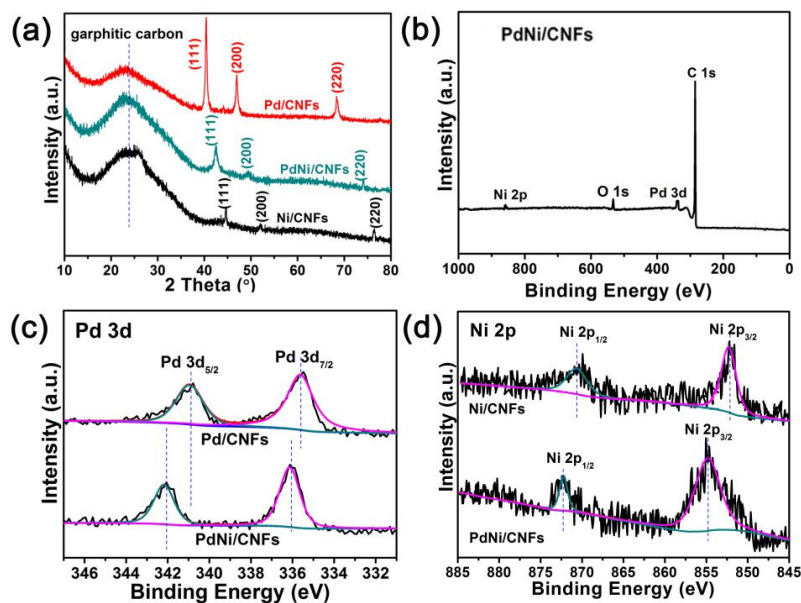PdNi/CNFs-1:2; (d) EDX line scans of the PdNi NPs.

Fig. 3 (a) XRD patterns of the Pd/CNFs, Ni/CNFs and PdNi/CNFs-1:2; (b) XPS survey spectrum

of PdNi/CNFs-1:2; (c) Pd 3d XPS spectra of the Pd/CNFs and PdNi/CNFs-1:2; (d) Ni 2p XPS

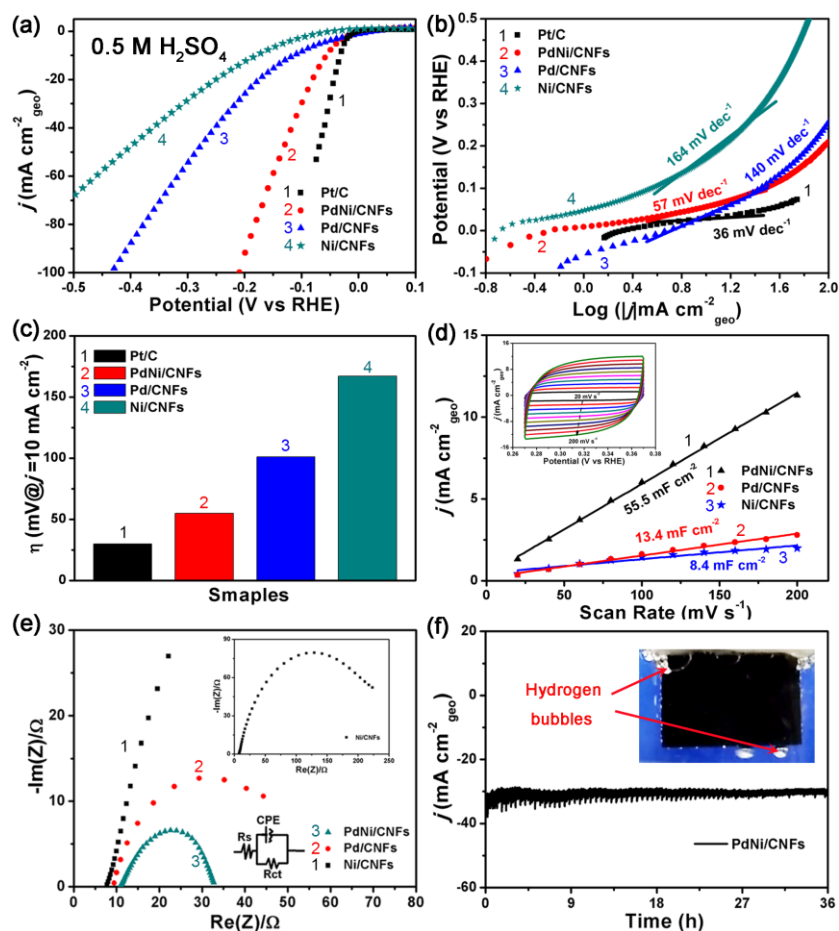spectra of the PdNi/CNFs-1:2 and Ni/CNFs.

Fig. 4 HER electrocatalysis in 0.5 M H_2SO_4. (a) Polarization curves and (b) corresponding Tafel plots of the Pd/CNFs, Ni/CNFs, PdNi/CNFs-1:2 and commercial Pt/C catalyst; (c) Histograms of overpotentials at j =10 mA cm^{-2} for the catalysts of Pd/CNFs, Ni/CNFs, PdNi/CNFs-1:2 and commercial Pt/C; (d) The linear fit of the capacitive currents of the catalysts *vs.* the scan rates, inset in (d) is the electrochemical cyclic voltamograms of Pd/CNFs at potential scanning rates from 20 mV s^{-1} to 200 mV s^{-1}; (e) EIS of the Pd/CNFs, Ni/CNFs and PdNi/CNFs-1:2 at the potential of -0.1 V vs RHE (the insets show the equivalent circuit of the fitted curves and the full EIS spectrum of the Ni/CNFs); (f) chronoamperometric response (j-t) curve of PdNi/CNFs-1:2 at a constant voltage of 50 mV vs RHE (the insets show a digital image of the H_2 bubbles formed on the PdNi/CNFs-1:2 membrane during the electrocatalytic process).
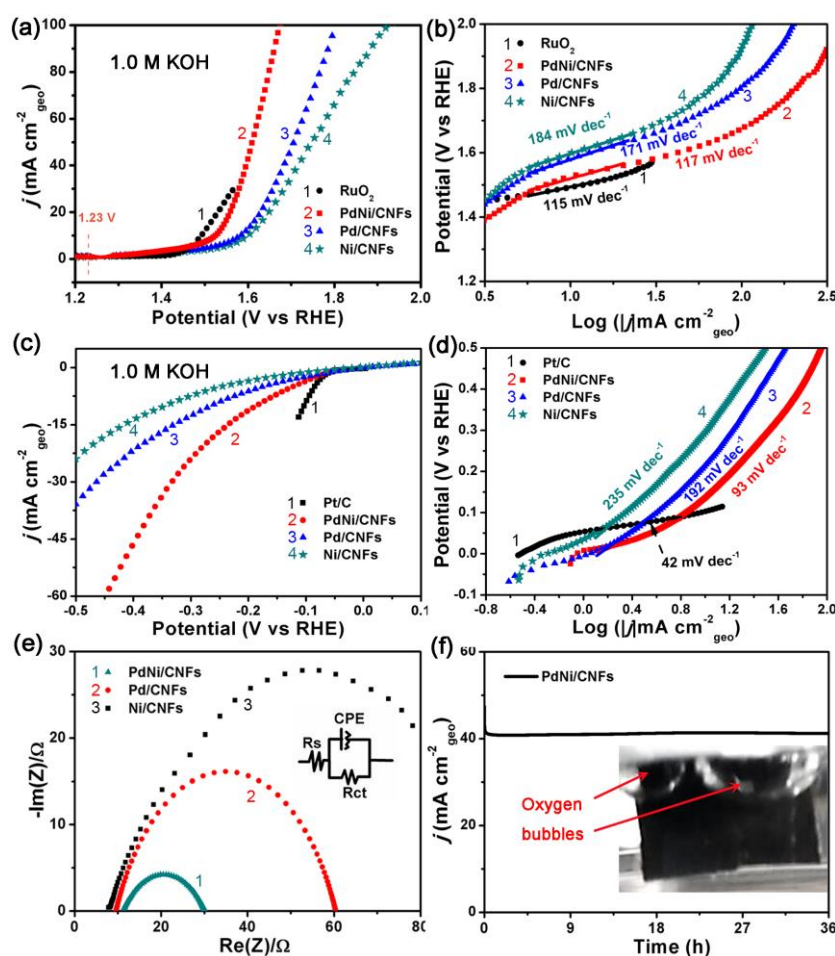
Fig. 5 OER and HER electrocatalysis in 1 M KOH. (a) Polarization curves and (b) corresponding

Tafel plots of the Pd/CNFs, Ni/CNFs, PdNi/CNFs-1:2 and commercial RuO_2 catalyst for OER; (c)

Polarization curves and (d) corresponding Tafel plots of the Pd/CNFs, Ni/CNFs, PdNi/CNFs-1:2

and commercial Pt/C catalyst for HER in 1 M KOH electrolyte; (e) EIS of the Pd/CNFs, Ni/CNFs

and PdNi/CNFs-1:2 at the potential of 1.60 V vs RHE (the inset shows the equivalent circuit of the

fitted curves); (f) chronoamperometric response (j-t) curve of PdNi/CNFs-1:2 at a constant

potential of 1.60 V vs RHE (the inset shows a digital image of the O_2 bubbles formed on the

PdNi/CNFs-1:2 membrane during the electrocatalytic process).

Table 1 Electrocatalytic properties of the prepared catalysts.

			η@10 mA cm^{-2} (mV)	Tafel slope (mV dec^{-1})	j$_0$ (mA cm^{-2})	Cdl (mF cm^{-2})	OCP (V)
Pd/CNFs	**0.5 M H$_2$SO$_4$**	HER	101	140	0.678	13.4	0.09
	1.0 M KOH	OER	348	171	/	/	1.46
		HER	265	192	/	/	0.07
Ni/CNFs	**0.5 M H$_2$SO$_4$**	HER	167	164	0.211	8.4	0.02
	1.0 M KOH	OER	380	184	/	/	1.48
		HER	345	235	/	/	0.07
PdNi/CNFs-1:0.5	**0.5 M H$_2$SO$_4$**	HER	120	155	0.423	/	0.04
	1.0 M KOH	OER	385	351	/	/	1.32
		HER	323	185	/	/	0.04
PdNi/CNFs-1:1	**0.5 M H$_2$SO$_4$**	HER	79	109	0.968	/	0.08
	1.0 M KOH	OER	312	256	/	/	1.22
		HER	266	173	/	/	0.05
PdNi/CNFs-1:2	**0.5 M H$_2$SO$_4$**	HER	55	57	1.536	55.5	0.06
	1.0 M KOH	OER	289	117	/	/	1.40
		HER	187	93	/	/	0.04
PdNi/CNFs-1:4	**0.5 M H$_2$SO$_4$**	HER	49	90	1.123	/	0.05
	1.0 M KOH	OER	340	158	/	/	1.46
		HER	219	135	/	/	0.06

Table 2 Electrochemical parameters relating to the EIS pattern.

		Potential (V vs RHE)	Rct (Ω)	Q(CPE) (n)	Qdl (F)
Pd/CNFs	HER	-0.10	47	0.76	0.0043
	OER	1.60	52	0.72	0.0065
Ni/CNFs	HER	-0.10	321	0.71	0.0029
	OER	1.60	89	0.76	0.0037
PdNi/CNFs-1:2	HER	-0.10	23	0.79	0.0176
	OER	1.60	19	0.75	0.0265

31